Assessing the implications of tectonic compaction on pore pressure using a coupled geomechanical approach

Joshua Obradors-Prats[a], Mohamed Rouainia[a], Andrew C. Aplin[b] and Anthony J.L. Crook[c]

[a]*School of Civil Engineering and Geosciences, Newcastle University, Newcastle upon Tyne, NE1 7RU, UK*
[b]*Department of Earth Sciences, Durham University, Durham, DH1 3LE, UK*
[c]*University of Leeds, LS2 9JT, UK*

Abstract

Overpressure prediction in tectonic environments is a challenging topic. The available pore pressure prediction methods are designed to work in environments where compaction is mostly one dimensional and driven by the vertical effective stress applied by the overburden. Furthermore, the impact of tectonic deformation on stresses, porosity and overpressure is still poorly understood. We use a novel methodology to capture the true compaction phenomena occurring in an evolving 3D stress regime by integrating a fully-coupled geomechanical approach with a critical state constitutive model. To this end, numerical models consisting of 2D plane strain clay columns are developed to account for compaction and overpressure generation during sedimentation and tectonic activity. We demonstrate that a high deviatoric stress is generated in compressional tectonic basins, resulting in a substantial decrease in porosity with continuing overpressure increase. The overpressure predictions from our numerical models are then compared to those estimated by the equivalent depth method (EDM) in order to quantify the error induced when using classical approaches, based on vertical effective stress, in tectonic environments. The stress paths presented here reveal that a deviation from the uniaxial burial trend can substantially reduce the accuracy of the EDM overpressure predictions.

Keywords: Tectonic compaction, overpressure, equivalent depth method (EDM), coupled geomechanics, critical state, finite element

1. Introduction

During the history of a sedimentary basin the clay sediments may experience different episodes since their deposition including burial, tectonic activity and diagenesis. These episodes trigger physical and chemical processes which have a great influence on sediment properties and the resulting transient pore pressure field (Osborne and Swarbrick, 1997; Wangen, 2001; Swarbrick et al., 2002). The physical processes are termed as mechanical compaction which accounts for porosity loss caused by the change in effective stresses, sediment strength and compressibility (Gutierrez and Wangen, 2005). On the other hand, chemical compaction encompasses all the chemical processes occurring in sediments during digenesis including mineral dissolution and precipitation.

In this paper, chemical compaction is neglected and attention is focused only on mechanical compaction, which may result from both the increasing vertical stress during burial, and the increase in lateral stresses resulting from tectonic deformation. Compaction of sediments requires fluid flow outward from the void spaces as the rock volume and porosity decrease. If the velocity of fluid escaping from the pores is too low, relative to the compressive load rate, part of the load will be carried by the fluid. As a result, the pore pressure will increase and the sediments will become overpressured (the pore pressure will be higher than the hydrostatic pressure). This overpressure generation mechanism is known as disequilibrium compaction. In the present paper two types of disequilibrium compaction are distinguished: disequilibrium compaction due to (1) ineffective dewatering during burial and (2) the tectonic induced overpressures resulting from ineffective dewatering during tectonic compressive deformation.

Knowledge of the pore pressure in the subsurface is a valuable tool for many applications within the oil industry that can help to minimize costs and risks. For example, it is used to design drilling mud weight programs and well casings. Furthermore, it can provide valuable information to assess fluid migration pathways, trap volumes and seal trap integrity (Brown and P., 2008). In addition, high overpressures may play a role in fault formation and can facilitate structural detachments (Hubbert and Rubey, 1959; Corredor et al., 2005; Krueger and Grant, 2011). Thus understanding of the sub-surface pore pressure regime could potentially help geological structural interpretations.

Therefore, pore pressure prediction is a topic of great interest for a wide scientific community of different disciplines. Because accuracy is crucial, several techniques are commonly used in combination to reduce uncertainty in predictions. Two main approaches are used for pore pressure prediction: (1) porosity-based methods which depend on rock property relationships and the analysis of the trends with depth (Van Ruth et al., 2002; Yang and Aplin, 2004; Bera, 2010; Zhang, 2011) and (2) forward basin modelling (Schneider et al., 1996; Bekele et al., 2001; Schneider and

Hay, 2001; Bolås et al., 2004; Allwardt et al., 2009; Hantschel and Kauerauf, 2009; Neumaier et al., 2014), which provides numerical simulations of different physical and chemical mechanisms of overpressure generation and dissipation during basin evolution and therefore is capable of capturing pore pressure history over geologic times. The main limitation of both approaches is that the adopted mechanical compaction models are unidimensional and based on the vertical effective stress. Therefore, the impact of tectonic activity on sediment properties and pore pressure generation is not accurately captured by these methods which may result in significant inaccuracies in estimates of pore pressure in tectonic environments (Hennig et al., 2002; Swarbrick, 2002).

Geomechanical modelling can be employed in conjunction with advanced constitutive models to simulate sediment rheology which are capable of accounting for the full 3D stress tensor and its impact on compaction (Albertz and Lingrey, 2012; Albertz and Sanz, 2012; Luo et al., 2012; Smart et al., 2012) and overpressure generation (Nikolinakou et al., 2012; Thornton and Crook, 2014).

In this paper, we present fully coupled, 2D plane strain geomechanical models using the finite element method to solve the governing equations for the mechanical and fluid flow fields. The models consider the sedimentation, burial, compaction, fluid flow and tectonic deformation during the history of a basin. It should be pointed out that the development of deformation structures resulting from tectonic activity as folds and thrusts are not considered in the numerical models. With the present work we aim to: (i) provide a qualitative and quantitative understanding of the impact of tectonic deformation on sediment properties, stresses and overpressure and (ii) quantify the inaccuracy of the classical pore pressure prediction methods in tectonic environments. To this end, a parametric study has been undertaken to analyse the effect of basin history on the final observed overpressures and to elucidate the main factors that lead to the failure of overpressure prediction methods.

2. Modelling approach

The Finite Element software ParaGeo (Crook, 2013) has been used to create the numerical models. Both fully implicit and quasistatic explicit algorithms are implemented in the software for solving the governing equations which are described in the following section.

2.1. Governing equations

The work presented in this paper adopts a fully-coupled staggered sequential approach to solve geomechanical and fluid flow equations taking into account the influence that these fields have on

each other at every coupling time step. The linear momentum balance equation for a saturated medium containing a single fluid phase is written as (Lewis and Schreffler, 1998):

$$\boldsymbol{L}^T\left[\boldsymbol{\sigma}' + \alpha(\phi)\boldsymbol{m}p_f\right] + \rho_b \boldsymbol{g} = 0 \tag{1}$$

where $\boldsymbol{L}$ is the standard continuum mechanics differential operator, $\boldsymbol{\sigma}'$ is the effective stress tensor defined as:

$$\boldsymbol{\sigma}' = \left[\sigma'_x\ \sigma'_y\ \sigma'_z\ \tau_{xy}\ \tau_{yz}\ \tau_{zx}\right]^T \tag{2}$$

σ'_x, σ'_y and σ'_z are the normal stresses to orthogonal planes x, y and z respectively, τ_{yz}, τ_{zx} and τ_{xy} are the tangential stresses acting in planes x, y and z respectively, $\alpha(\phi)$ is the Biot's coefficient as a function of porosity, p_f is the pore fluid pressure and is the hydrostatic unit tensor, which is defined as:

$$\boldsymbol{m} = \left[1\ 1\ 1\ 0\ 0\ 0\right]^T \tag{3}$$

ρ_b is the saturated bulk mass density which is defined as:

$$\rho_b = (1-\phi)\rho_s + \phi\rho_f \tag{4}$$

in which ρ_s and ρ_f are the solid and fluid densities respectively and $\boldsymbol{g}$ is the gravitational vector.

Effective stress is the component of the total stress exerted by the solid matrix. It is defined as:

$$\boldsymbol{\sigma}' = \boldsymbol{\sigma} - \alpha(\phi)\boldsymbol{p}_f \tag{5}$$

where $\boldsymbol{\sigma}$ is the total stress tensor.

For the current application we have assumed a constant value of $\alpha(\phi) = \alpha = 1$ which results in the Terzaghi's definition of the effective stress (Terzaghi, 1967). The fluid transport over geological time frames is modelled by the single phase Darcy's flow equation as defined in (Lewis and Schreffler, 1998):

$$\mathrm{div}\left[\frac{(\boldsymbol{k}(\phi)}{\mu_f}\left(\nabla p_f - \rho_f \boldsymbol{g}\right)\right] = \left[\frac{\phi}{K_f} + \frac{\left(\alpha(\phi) - \phi\right)}{K_s}\right]\frac{\partial p_f}{\partial t} + \frac{\alpha(\phi)}{(1-\phi)}\frac{\partial \phi}{\partial t} \tag{6}$$

where K_f is the fluid stiffness, K_s is the solid grains stiffness, μ_f is the fluid viscosity and $\boldsymbol{k}(\phi)$ is the permeability tensor which is a function of porosity. Note that the last term in Eq. 6 represents

the fluid flow due to a change in porosity and provides the coupling between the mechanical and flow fields.

2.2. Constitutive equations

The SR4 is a three-invariant rate-independent poro-elastic-plastic critical state constitutive model with non-associative plasticity. In the formulation, stress states are expressed by means of the effective mean stress p' and the deviatoric stress q defined as:

$$p' = \frac{\sigma'_1 + \sigma'_2 + \sigma'_3}{3},\ q = \sqrt{\frac{1}{2}\left[(\sigma'_1 - \sigma'_2)^2 + (\sigma'_1 - \sigma'_3)^2 + (\sigma'_2 - \sigma'_3)\right]^2} \tag{7}$$

where σ'_1, σ'_2 and σ'_3 are the three principal effective stresses.

2.3. Yield surface

The yield surface delimitates the domain of stress states that produce elastic and elastic-plastic strains (Fig. 1a). Stress paths moving inside the yield surface produce elastic deformation whereas stress paths that reach the yield surface produce elastic-plastic deformation. It is defined in the $p' - q$ plane with two functions that intersect at the point of maximum deviatoric stress. The shear side is defined using the SR3 surface (Crook et al., 2006) whereas the compression side is defined by the elliptical function of the standard Cam clay model (Wood, 1990; Rouainia and Muir Wood, 2000):

$$\phi(p', \varepsilon_v^p) = g(\theta, p')q + (p' - p_t)\tan\beta\left[\frac{(p' - p_c)}{(p_t - p_c)}\right]^{1/n} \tag{8}$$

for $p' \geq p_{\phi_{peak}}$ and

$$\phi(p', \varepsilon_v^p) = \left[g(\theta, p')\right]^2 q^2 - M_\phi^2 p_{\phi_{peak}}^2\left[1 - \frac{(p_{\phi_{peak}} - p')^2}{(p_{\phi_{peak}} - p_c)^2}\right] \tag{9}$$

for $p' < p_{\phi_{peak}}$

where p_t is the tensile intercept of the yield surface with the hydrostatic axis, p_c is the pre-consolidation pressure or compressive intercept of the yield surface with the hydrostatic axis, $p_{\phi_{peak}}$ is the effective mean stress at q peak value, ε_v^p is the plastic volumetric strain, M_ϕ is the slope of the line that intersects both the origin of the $p' - q$ space and the yield surface in q peak value, β and n are material constants which define the shape of the yield surface in the $p' - q$ plane, θ is the lode angle and $g(\theta, p')$ is a function that controls the shape of the yield surface in the deviatoric plane (plane normal to hydrostatic axis as seen in Fig. 1b) and is computed as:

$$g(\theta, p') = \left[\frac{1}{1-\beta^{\pi}(p')} \left(1+\beta^{\pi}(p')\sin(3\theta)\right) \right]^{N^{\pi}} \tag{10}$$

where N^{π} is a deviatoric plane shape material constant and $\beta^{\pi}(p')$ is a function defined as (Desai and Salami, 1987):

$$\beta^{\pi}(p') = \beta_0^{\pi} \exp\left(\beta_1^{\pi} p' \frac{p_{c0}}{p_c}\right) \tag{11}$$

where β_0^{π} and β_1^{π} are material constants and p_{c0} is the initial pre-consolidation pressure (corresponding to uncompressed and undamaged material).

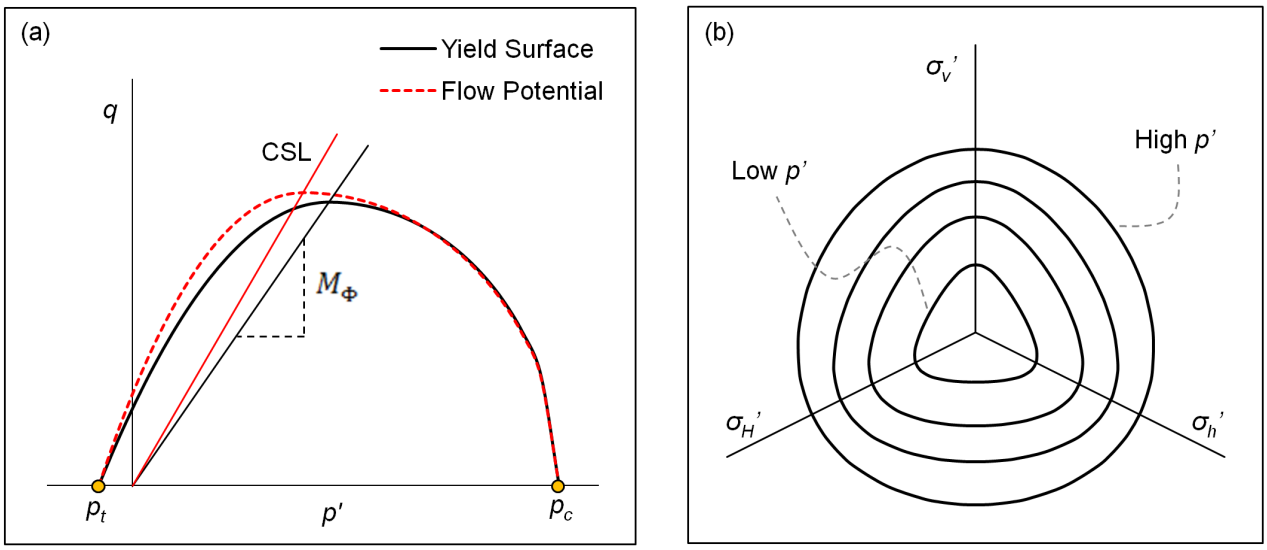

Figure 1: SR4 constitutive model: (a) the yield surface and flow potential plotted in the $p'-q$ plane and (b) the yield surface plotted in the deviatoric plane for different values of mean effective stress p'.

2.4. Flow potential

The flow potential surface has the same form of the state boundary surface but is defined with two different parameters. This enables the critical state line (CSL) to be defined to intersect the state boundary surface on the shear side, as opposed to the peak stress, which is consistent with experimental observations for clays (Cotecchia and Chandler, 1997; Ventouras and Coop, 2009). The flow potential surface is defined as:

$$\psi(p', \varepsilon_v^p) = q + (p' - p_t)\tan\psi \left[\frac{(p'-p_c)}{(p_t-p_c)} \right]^{(1/m)} \tag{12}$$

for $p' \geq p_{\psi_{peak}}$ and

$$\psi(p',\varepsilon_v^p) = q^2 - M^2 p_{\psi_{peak}}^2 \left[1 - \frac{(p_{\psi_{peak}} - p')^2}{(p_{\psi_{peak}} - p_c)^2}\right] \tag{13}$$

for $p' < p_{\psi_{peak}}$

where M is the slope of the critical state line, $p_{\psi_{peak}}$ is the effective mean stress corresponding to the peak value of q for the flow potential surface, and ψ and m are material constants which define the shape of the flow potential surface in the $p' - q$ plane. Note that the flow potential surface does not have any deviatoric correction term (as opposed to the yield surface) as it is circular in the deviatoric plane for all values of p_c.

2.5. Hardening law

The CSL divides the yield surface in the regions of compaction and dilation. Stress paths that reach the yield surface on the compression domain will cause a diffuse volumetric plastic strain and an increase in both, pre-consolidation pressure and yield surface size (strength increase or hardening) whereas stress paths that reach the yield surface on the dilation domain will cause a shear localization with volume increase and a decrease in both, pre-consolidation pressure and yield surface size (strength decrease or softening). Continuous shearing in critical state induces shear plastic strain at constant volume. The hardening and softening of materials is controlled by the hardening law which is defined as a function of the plastic volumetric strain:

$$p_c(\varepsilon_v^p) = p_{c0} \exp\left(-\frac{\nu \varepsilon_v^p}{\lambda - \kappa}\right) \tag{14}$$

and

$$p_t(\varepsilon_v^p) = p_{t0} \exp\left(-\frac{\nu (\varepsilon_v^p)_{max}}{\lambda - \kappa}\right) \tag{15}$$

where ν is the specific volume and $\nu = 1 + e$, e is the void ratio, λ and κ are the slopes of the normal compression line (NCL) and unloading-reloading line in the $\nu - \ln p'$ plane and $(\varepsilon_v^p)_{max}$ is the maximum dilatational volumetric plastic strain.

2.6. Poroelasticity

Poro-elastic deformations rely on the existence of a non-linear porosity and stress state dependant function:

$$K = K_0 + (1 - A_{un})\frac{p_c}{\kappa} + A_{un}\frac{p'}{(1-\phi)\kappa} \tag{16}$$

where K is the bulk modulus, p_c is the pre-consolidation pressure, K_0 is the bulk modulus at deposition (i.e. when $p_c \to 0$ and $\sigma'_m \to 0$), κ is the elastic unloading modulus, ϕ is the porosity and A_{un} is the dependence factor which have values $0 \leq A_{un} \leq 1$.

The standard Cam clay poroelastic law has a limited applicability in field scale cases because the slope of the swelling line is independent of the maximum stress experienced by the sediments. Note that the volume change for a given stress increment is expected to be small in sediments that have been subjected to a large maximum stress in the past; for example sediments with low porosity (Hashiguchi, 1995). To overcome that limitation Equation (16) includes a pre-consolidation (and therefore porosity) dependent factor in the computation of the bulk modulus (first term of the right hand of the equation). Note that for $A_{un} = 1$ Equation (16) is identical to the standard Cam clay poroelastic law.

3. Numerical models

3.1. Description of models

The proposed numerical models involve different stages including sedimentation, lateral compression and post-tectonic sedimentation in a 2D plane strain clay column in order to simulate different basin histories (Fig. 2). The models start from an initial 1000 m wide and 400 m thick clay layer geometry. After the initialisation of the gravity forces, the sedimentation stage takes place consisting in the deposition of 10 clay layers comprising a total thickness of 4000 m of sediment. Sedimentation rates of 100 m/Ma, 500 m/Ma and 2000 m/Ma were considered in order to define different disequilibrium compaction regimes (Table 1). After complete sedimentation, a uniform lateral deformation is assigned to the entire column by prescribing a displacement on the right boundary. Several combinations of displacement magnitude and duration were considered resulting in different percentages of shortening (5%, 10% and 20%) and different shortening rates (100 m/Ma, 200 m/Ma and 400 m/Ma). The cases D1, D2 and D3 also encompass a final stage in which a 500 m thick clay layer is deposited subsequent to the tectonic event at sedimentation rates of 100 m/Ma, 500 m/Ma and 2000 m/Ma, respectively.

di!erent initial stress states and initial locations

The typical material parameters and porosity-permeability curve, which have been used to simulate the clay constitutive behaviour, are shown in Table 2 and Fig. 3, respectively. Note that permeability is defined to be a function of porosity using the Yang and Aplin (2010) model.

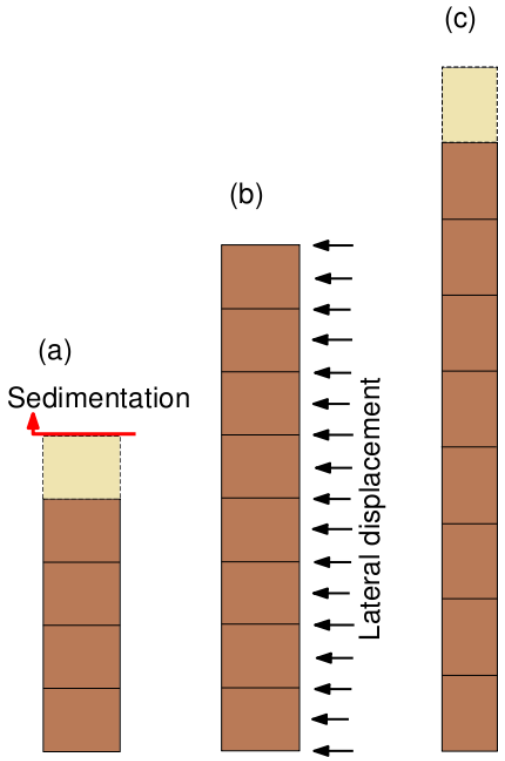

Figure 2: Different loading stages applied to the numerical models: (a) sedimentation, (b) lateral compression and (c) post-tectonic sedimentation.

Table 1: Summary of the cases simulated with specification of the varied parameters. Note that cases A2, B2 and C2 are identical but are designed with different label for the sake of clarity.

Case	Sedimentation rate (m/Ma)	Shortening (%)	Shortening rate (m/Ma)	Sedimentation rate after tectonic event (m/Ma)
O1	100	-	-	-
O2	500	-	-	-
O3	2000	-	-	-
A1	100	-	-	-
A2	500	10	200	-
A3	2000	-	-	-
B1	-	5	-	-
B2	500	10	200	-
B3	-	10	-	-
C1	-	-	100	-
C2	500	10	200	-
C3	-	-	400	-
D1	-	-	-	100
D2	500	10	200	500
D3	-	-	-	2000

Table 2: Material parameters for the clay lithology with a clay fraction of 40%. The yield surface and flow potential were defined with an adequate critical state friction angle for the lithology (c.a. 20^o). The hardening parameters were defined so that the porosity trend under hydrostatic conditions fits the data for Gulf of Mexico sediments in Hudec et. al. (2009).

Description	Symbol	Value
Yield surface $p' - q$ plane	p_{c0} (MPa)	0.1
	p_t (MPa)	-0.01
	β (^{o})	55
	n	1
Yield surface deviatoric plane	N^p	0.25
	β_0^p	0.6
	β_1^p	0.6
Flow potential surface	ψ (^{o})	60
	m	0.8
Hardening law and elasticity	K_0 (MPa)	10
	ϕ_0 (%)	58
	λ	0.205
	κ	0.02
	A_{un}	0.5
Grain properties potential	ρ_s (kg/m^3)	2650
Fluid properties	ρ_f (kg/m^3)	1000
	k_f (MPa)	2000
	μ_f (MPa·Ma)	3.171×10^{-23}

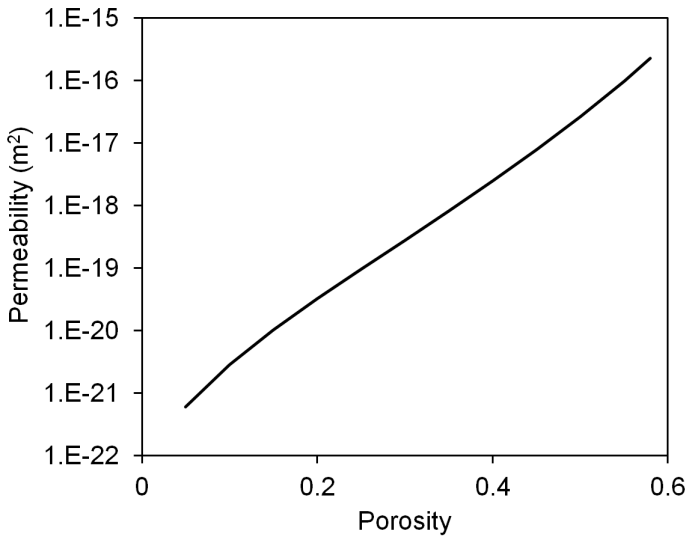

Figure 3: Clay porosity-permeability relationship using Yang and Aplin (2010) model with CF=0.4.

3.2. Numerical modelling aspects

Lagrangian and Eulerian reference frames are used for the mechanical and fluid phases respectively; i.e. fluid flow is relative to the deformation of the FE mesh for the solid phase. A finite strain formulation is used based on the well-established multiplicative split of the deformation gradient (e.g. Peric and Crook, 2004).

The FE mesh consists of unstructured triangular elements with an average size of 50 m. An average volume strain formulation is used to overcome volumetric locking associated with constant volume deformation at/near critical state. In order to avoid excessive mesh distortion and premature termination of the calculations, an automatic remeshing procedure is triggered once the element area is distorted by 10%. The remeshing procedure also facilitates the simulation of sedimentation by updating the mesh to account for the new material each time a layer is deposited.

The time discretisation has been defined in each model according to the total simulation time in such a way that a similar number of time steps is used to solve a given stage (i.e. sedimentation, tectonic deformation or post tectonic burial) in all models. For example, case O2, which comprises 8 Ma of sedimentation, has been solved using a mechanical time step of 2.0×10^{-5} Ma and a flow step (coupling step) of 0.02 Ma. This is equivalent to a total number of 4.0×10^{5} mechanical steps and 400 flow steps for the full simulation time, which corresponds to 1000 mechanical steps for each flow step.

4. Results

In the next section, the modelling results for the parametric study described in Table 1 are presented. Note that for the sake of clarity and better quantification of the effect of the investigated parameters some results for the cases accounting for tectonic activity are expressed as the increment relative to the corresponding parent case (the case with identical parameters in the previous stages). For example, rather than plotting overpressure with depth for case B1, the results are expressed as overpressure increment computed as the overpressure in case B1 minus the overpressure in O2 for each depth and consequently the legend for the presented curve will be labelled as B1 - O2.

4.1. EDM error quantification approach

It is widely known that vertical effective stress based techniques for overpressure prediction, known as the Equivalent Depth Method (EDM), are only accurate in basins where vertical burial stresses drive disequilibrium compaction for overpressure generation, however, when other stresses

(tectonic compaction) or other mechanisms such as chemical compaction and fluid expansion are involved, the techniques fail and overpressure is usually underestimated (Swarbrick, 2002). A principal aim of this study is to quantify the error in estimates of overpressure when using the EDM in regions subjected to tectonic activity. For this purpose the same approach as in Obradors-Prats et al. (2016) is adopted: porosity predictions from the numerical models are compared to the normal compaction trend (NCT) to predict overpressure using the EDM. Then the error is computed as the difference between the overpressure predicted by the numerical models and that obtained by means of the EDM. It should be highlighted that in the present work the sedimentation and tectonic events are sequential rather than synchronous as in Obradors-Prats et al. (2016). When tectonic deformation occurs after complete sedimentation this tends to induce a notable porosity loss in sediments. As a result, the porosity trend in the shallow sediments might fall to the left of the original NCT. Given that a basic assumption of the EDM is that the NCT should fit the porosity data in the shallow section (where sediments are assumed to be hydrostatic), the original NCT should be corrected prior to the application of the EDM. Without correction, the EDM would predict underpressure in the shallow sediments. In Fig. 4 the NCTs before and after the correction are shown.

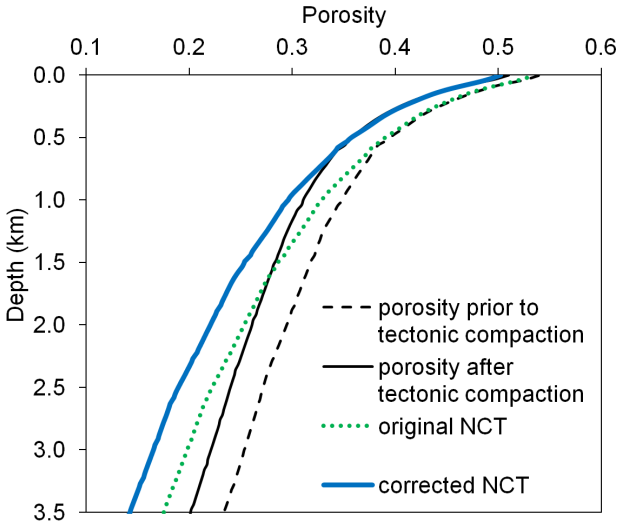

Figure 4: Example of the NCT correction approach to account for the porosity loss due to tectonic compaction. The original NCT is shifted to the left to match the porosity trend in shallow sediments before the application of the EDM. Note that if the original NCT is used for the application of the EDM in the tectonically compacted sediments, underpressure would be predicted for depths up to c.a. 1.5 km (where the porosities of the compacted sediments lie to the left of the original NCT).

4.2. Results after sedimentation

The cases O1, O2 and O3 only consider the sedimentation stage during which 4000 m of sediment is deposited at sedimentation rates of 100 m/Ma, 500 m/Ma and 2000 m/Ma, respectively.

These cases constitute the parent cases for the rest of the simulations and therefore are selected as benchmarks for analysing the effect of the different basin histories on stresses, pore pressure and porosity.

The simulation results show that the faster the sedimentation rate the higher the overpressure generated by disequilibrium compaction (Fig. 5a). Pore pressure reaches magnitudes of 39.9 MPa in case O1, 46.9 MPa in case O2 and 52.9 MPa in case O3 at 3.5 km depth that is equivalent to overpressures of 5.7 MPa, 12.8 MPa and 18.8 MPa, respectively. Overpressure decreases the effective stresses acting on sediments and hinders compaction. Therefore, the faster the sedimentation rate, the better the porosity preservation (Fig. 5b). (Fig. 5c) shows the final permeability versus depth for each case.

4.3. Effect of the shortening percentage

Comparison of the cases B1, B2 and B3 aims to illustrate the effect of the amount of shortening on sediment stresses, porosity and overpressure along with the quantification of the error resulting from EDM overpressure prediction. O2 is the parent case for B1, B2 and B3 with a sedimentation stage at a constant deposition rate of 500 m/Ma. Once the sedimentation is complete, a prescribed displacement was applied to the right hand boundary considering displacement magnitudes of 50 m, 100 m and 200 m resulting in 5%, 10% and 20% of shortening, respectively. The duration of the displacement was defined to maintain a constant shortening rate of 200 m/Ma in all the cases.

It is not difficult to anticipate that the tectonically induced overpressure increases as the amount of shortening increases. The results in Fig. 6a show an increase in overpressure which amounted to 16.4 MPa, 12.3 MPa and 9.3 MPa at 3.5 km depth for cases B3, B2 and B1, respectively. The differences in the magnitude of the tectonically induced overpressure between the three cases increase with depth due to the decrease of permeability with depth.

Fig. 6b shows the increments versus depth of the vertical effective stress, σ'_v, the maximum horizontal effective stress, σ'_H, and the minimum horizontal effective stress, σ'_h. The horizontal shortening leads to an increase of the maximum total horizontal stress (σ_H). Part of the total stress is transferred to the solid matrix resulting in an increase in σ'_H and part is transferred to the pore fluid leading to an increase in the pore pressure. Therefore, for a given shortening, the increase in σ'_H depends on the pore pressure dissipation. The difference between cases B1, B2 and B3 in the σ'_H increment is larger between 0.5 and 2.5 km depth, but the differences are less evident at greater depths due to the contribution of the large tectonically induced overpressures. The increment in σ'_h for each case depends on the Poisson's ratio effect because of σ'_H and the overpressure. For depths below 2.4 km the cases B3 and B1 experienced the largest and the minimum increase in

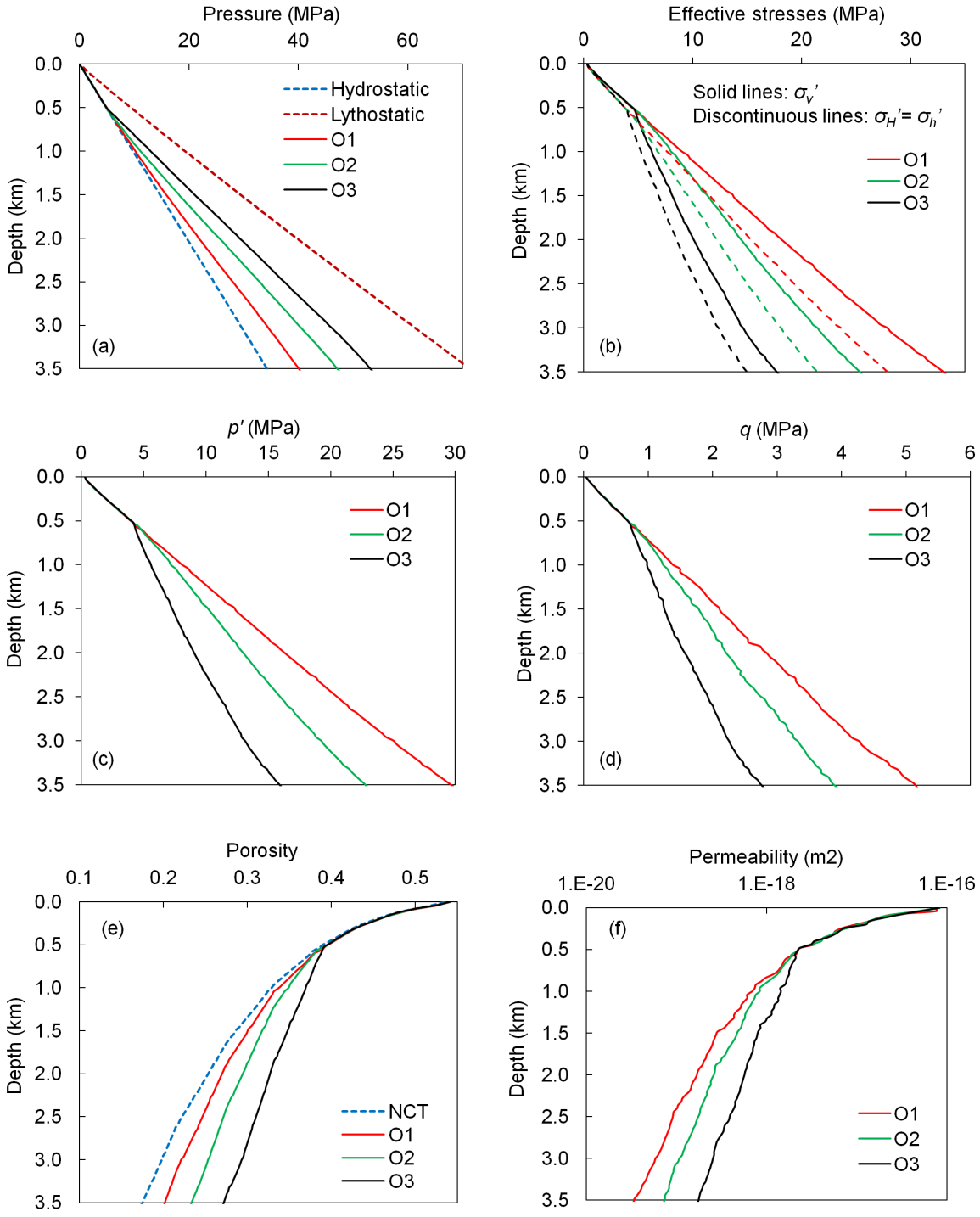

Figure 5: Results of cases O1, O2 and O3 after complete sedimentation: (a) pore pressure, (b) effective stresses, (c) effective mean stress, (d) deviatoric stress, (e) porosity and (f) permeability.

σ'_h respectively, whereas in depths above 2.4 km the trend is inverted. The change in σ'_v is mainly controlled by the increase in overpressure due to the tectonic event and the increase in density due to porosity reduction (Fig. 6e). The reduction in σ'_v reaches 10.5 MPa in case B3, 8.1 in case B2 and 6.5 in case B1 at 3.5 km depth.

The combination of the change in σ'_H, σ'_v and σ'_h (which are approximately in the direction of the three principal stresses) provide the change in the effective mean stress, p', and the deviatoric stress, q, shown in Figs. 6c and 6d. As expected, the larger the shortening the larger the increase in deviatoric stress which leads to a higher amount of shear enhanced compaction and porosity reduction. The application of EDM on the predicted porosity distributions leads to an underestimation of overpressure which increases with depth for all the cases. The error resulting from EDM predictions reach magnitudes of up to 10.6 MPa in case B3, 8.5 MPa in case B2 and 6.8 MPa in case B1 at 3.5 km depth. For all the cases the error resulting from the EDM predictions is lower than the overpressure increase. This is due to the overburden pressure correction inherent in the shifting of the NCT accounting for porosity loss due to tectonic compaction.

In Fig. 7 the stress paths for cases B1, B2 and B3 are presented. Note that the larger deviation of case B3 from the uniaxial strain line (K_0 path) is consistent with the larger error in the EDM prediction for same case.

4.4. Effect of shortening rate

For a given percentage of shortening the final observed pore pressures in a compressional basin depend on the relative rates of overpressure generation, which is directly related to the shortening rate (rate of the compressional loading), and overpressure dissipation (controlled by permeability and pore pressure gradient). Therefore, for a given permeability, the drainage in the basin is controlled by the shortening rate. As expected, the faster the shortening rate the larger the tectonically induced overpressure at present day. The increment in overpressure at 3.5 km depth has been 14.2 MPa, 12.3 MPa and 11.0 MPa for cases C3, C2 and C1 respectively (Fig. 8a). Given that the amount of shortening is the same for all the cases the differences in stress increments are attributed to differences in overpressure (Fig. 8b). In the hypothetical case of complete overpressure dissipation after the tectonic event, the solution will be identical for all the cases. Since pore pressure has no influence on the deviatoric stress, q, the solution for all the cases is identical and the difference in porosity loss after the tectonic event is attributed to the difference in p' (Figs. 8c, 8d and 8e). This results in a practically identical EDM prediction error for all the cases which reaches magnitudes of 8.5 ± 0.2 MPa at 3.5 km depth.

In Fig. 9 the stress paths for cases C1, C2 and C3 are presented. Note the similarity in the final stress states in all the cases. They only differ slightly in the effective mean stress magnitude and

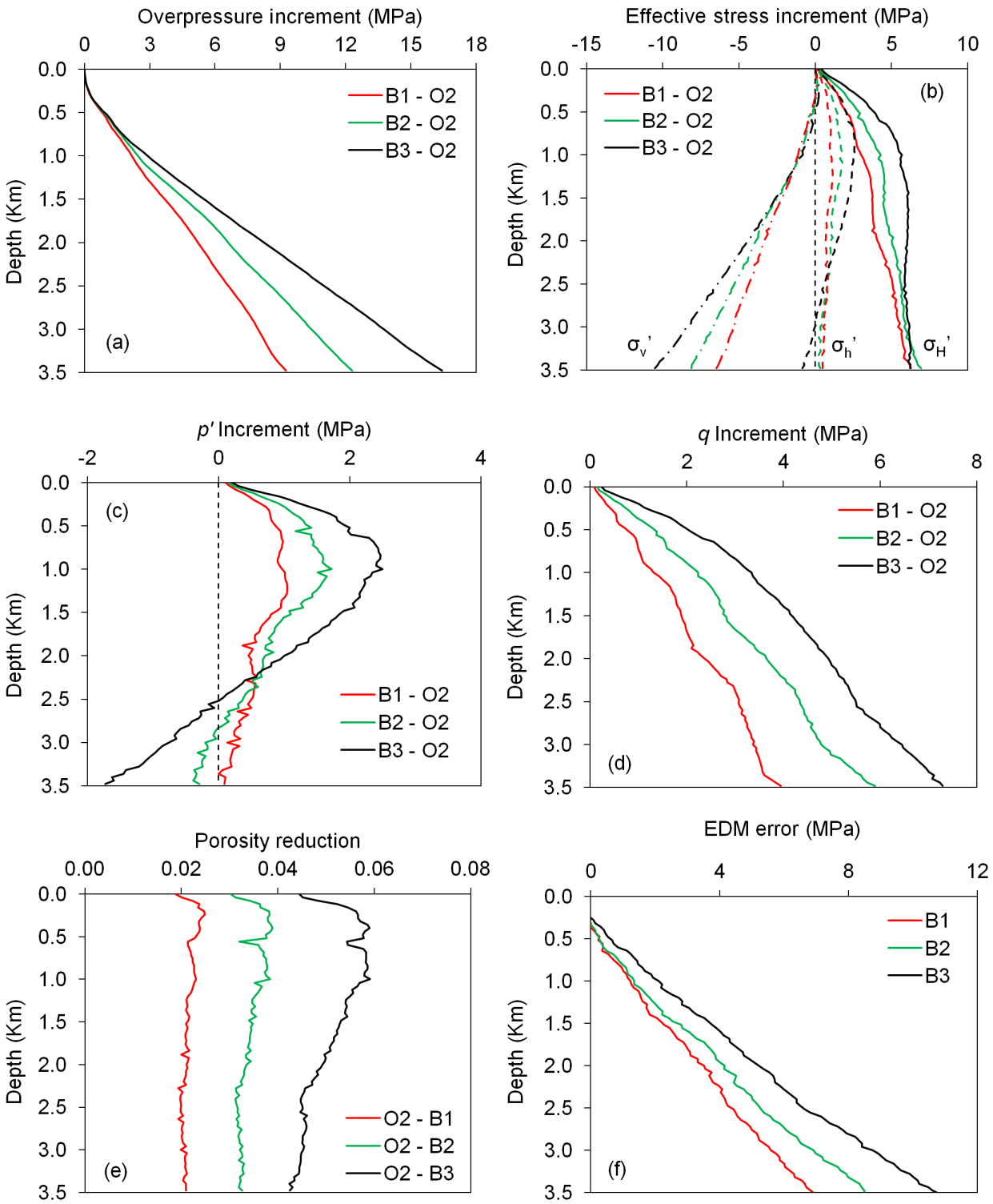

Figure 6: Results of cases B1, B2 and B3: (a) overpressure increment, (b) vertical and horizontal stresses increment, (c) effective mean stress increment, (d) deviatoric stress increment, (e) porosity reduction and (f) equivalent depth method error.

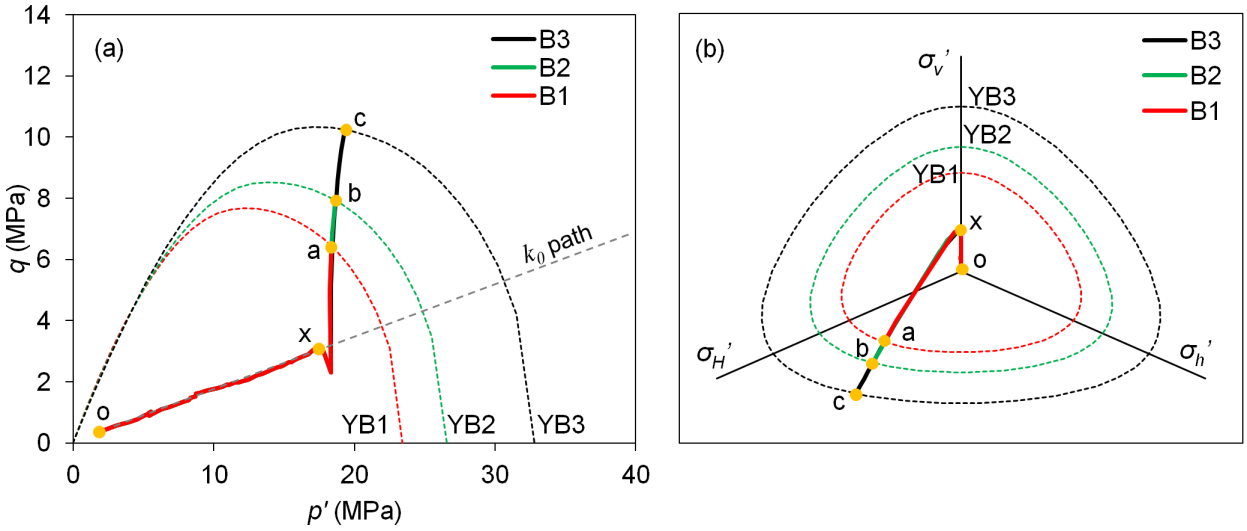

Figure 7: Results of cases B1, B2 and B3: (a) stress paths in the $p' - q$ plane and (b) stress paths in the deviatoric plane. The plots correspond to an element of rock situated at c.a. 2.8 km depth after sedimentation in each model. Point o is the initial stress state and point x is the stress state after the sedimentation stage for all the cases. Points a, b and c are the final stress states of cases B1, B2 and B3, respectively, and YB1, YB2 and YB3 are their corresponding final yield surfaces. The K_0 path is plotted for reference. The stress paths are described as follows: [o-x] burial trend at K_0 conditions, and [x - a/b/c] tectonic stress paths (the combined effects of a continuous decrease in σ_v' and an increase in σ_H' and σ_h' due to the tectonic event results in a decrease of q during an initial short period of time followed by an increase of q in the subsequent period). The comparison between all the cases reveals that the deviation (distance) from the K_0 path increases as the amount of shortening increases.

consequently the yield surface size (which is directly related to porosity). This is consistent with a similar EDM error magnitude for the three cases.

4.5. Effect of disequilibrium compaction

The cases A1, A2 and A3 aim to provide an insight on the behaviour of sediments under tectonic compaction depending on the compaction and pressure state prior to tectonic events. For such purpose, those cases consider an identical tectonic event (10% of shortening at 200 m/Ma shortening rate) acting on three columns deposited at different sedimentation rates (100 m/Ma, 500 m/Ma and 2000 m/Ma for A1, A2 and A3 respectively). Note that the parent cases for A1, A2 and A3 are O1, O2 and O3 respectively. The case A1 experienced the largest overpressure increase relative to its parent case O1 with a magnitude of 15.6 MPa at 3.5 km depth whereas in cases A2 and A3 overpressure increased up to 12.3 MPa and 9.2 MPa respectively (Fig. 10a). This behaviour is a consequence of the differences in permeability prior to the tectonic event (Fig. 5c). The lower permeability in the case O1 hindered to a greater extent the dissipation of the tectonically induced overpressures during the tectonic event compared to the other cases with larger permeabilities. Because all the cases are subjected to an identical tectonic event, the porosity loss is quite similar and it ranges between 3 and 4 porosity units with a maximum difference of one porosity unit at 0.5 km depth. The resulting porosity trends after the tectonic event are shown in Fig. 10c together

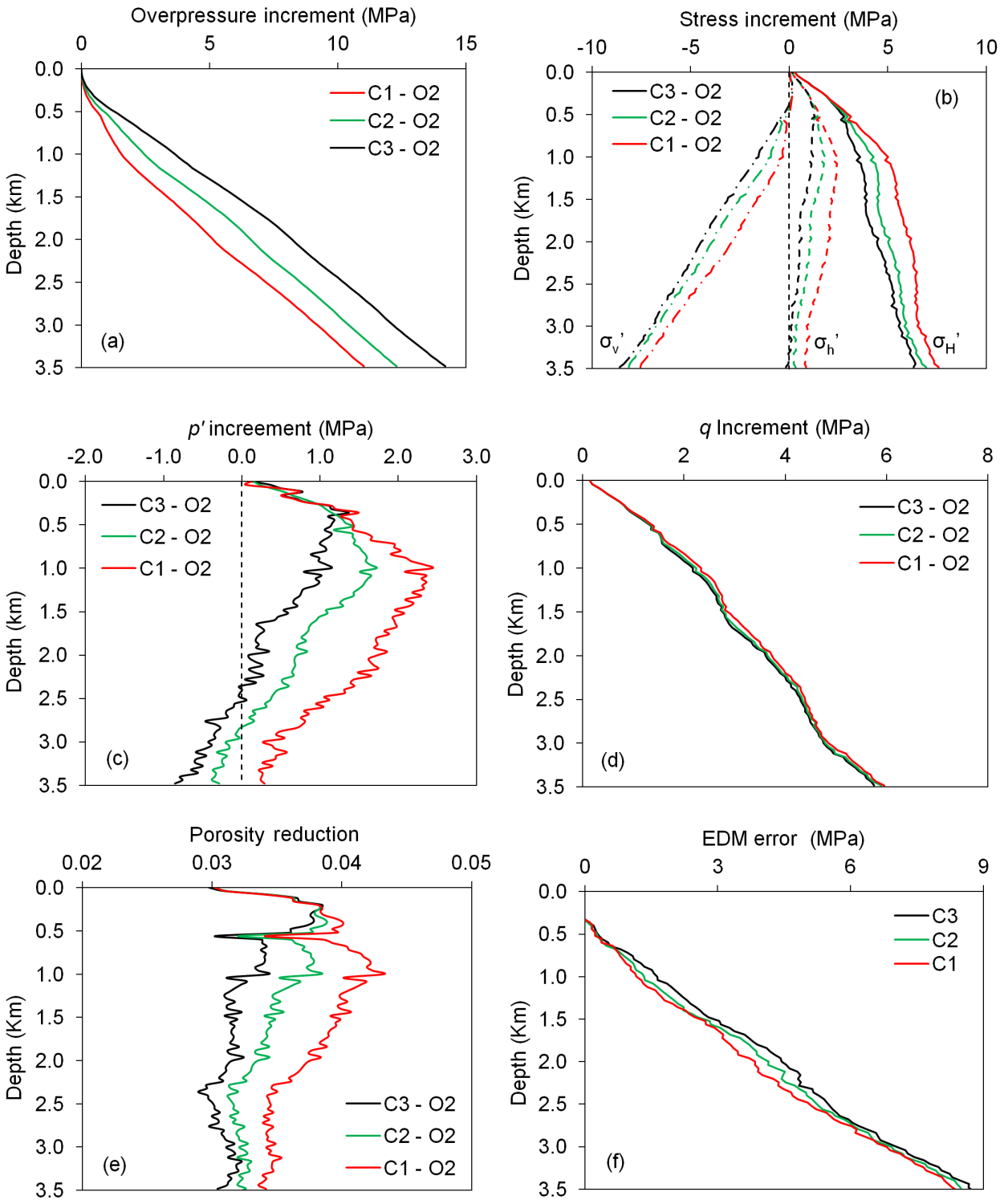

Figure 8: Results of cases C1, C2 and C3: (a) overpressure increment, (b) vertical and horizontal stresses increment, (c) effective mean stress increment, (d) deviatoric stress increment, (e) porosity reduction and (f) equivalent depth method error.

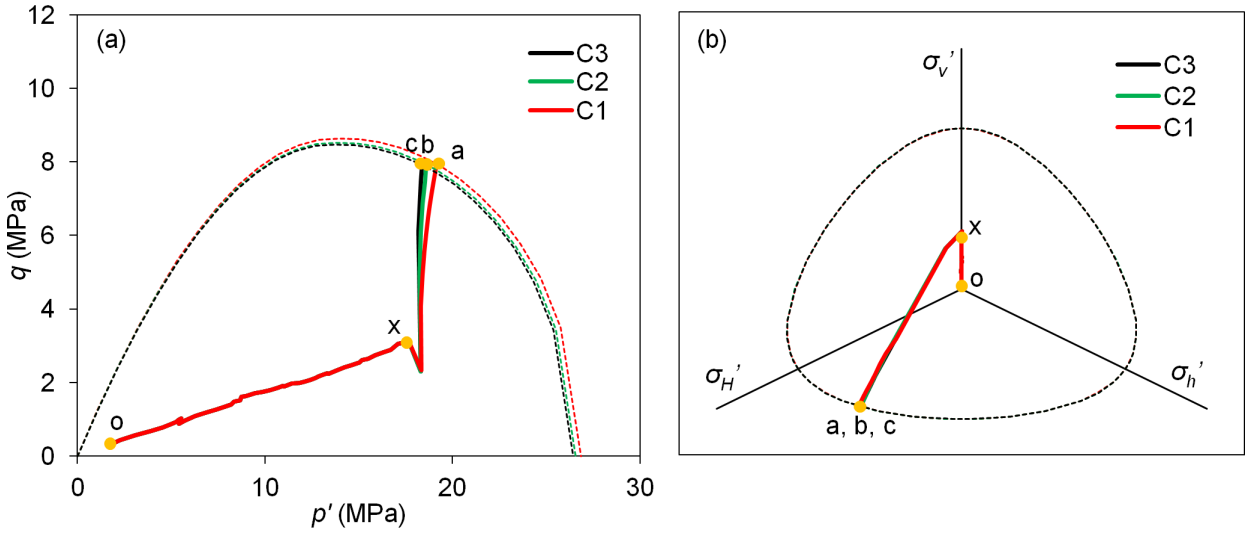

Figure 9: Results for cases C1, C2 and C3: (a) stress paths in the $p' - q$ plane and (b) stress paths in the deviatoric plane. The plots correspond to an element of rock situated at c.a. 2.8 km depth after sedimentation in each model. Point o represents the initial stress state and point x is the stress state after the sedimentation stage for all the cases. Points a, b and c are the final stress states for cases C1, C2 and C3, respectively. Their corresponding final yield surfaces are plotted with the same colour but are not labelled in the plot for the sake of clarity. The stress paths are described as follows: [o-x] burial trend at K_0 conditions, and [x - a/b/c] tectonic stress paths. Note that the different shortening rates in all the cases have a negligible effect on the final stress states (with the exception of small differences in the mean effective stress).

with the original NCT and the corrected NCT accounting for tectonic compaction. The application of the EDM using porosity trends results in higher overpressure underestimation as there is less disequilibrium compaction prior to the tectonic event. The magnitude of the EDM error reached 11.1 MPa, 8.5 MPa and 5.5 MPa at 3.5 km depth for cases A1, A2 and A3 respectively.

This results can be explained by two facts: (1) The case with less disequilibrium compaction had the lowest permeability prior to the tectonic event what resulted in a larger increase in tectonically induced overpressure and (2) The case with less disequilibrium compaction had the porosities closer to the NCT compared to the other cases prior to the tectonic event and because porosity loss is quite similar in all the cases, this results in an overpressure prediction by the EDM which is low compared to the true overpressure magnitude.

The stress paths for the three cases are presented in Fig. 11. The relatively low overpressure and low porosity of case A1 after the sedimentation stage facilitated more overpressure development during the tectonic stage than in cases A2 and A3. This resulted in the highest decrease of σ'_v out of the three cases and therefore more deviatoric stress development. Consistent with the highest EDM error magnitude, the final stress state of A1 shows the largest deviation from the 1D compaction trend (K_0 path).

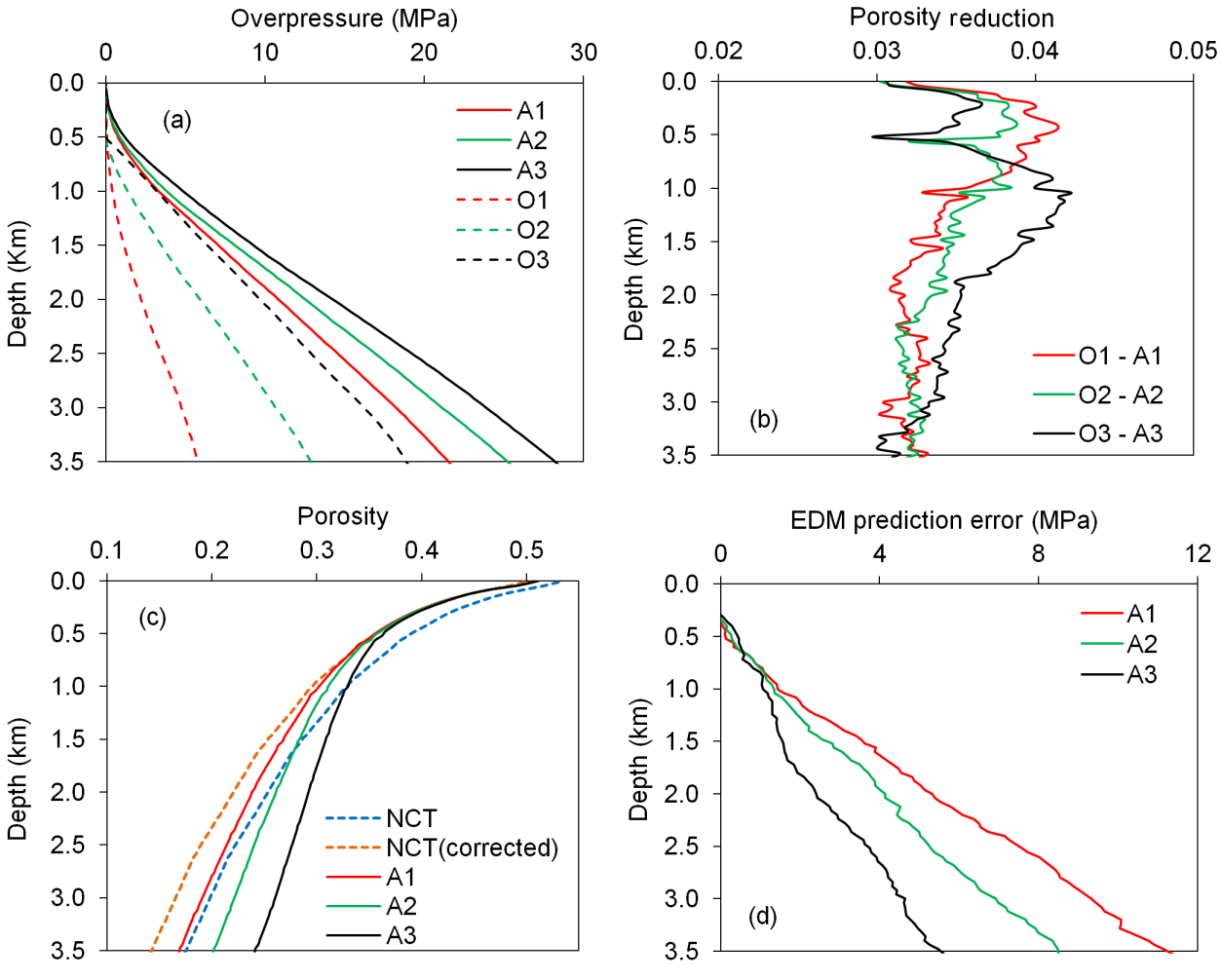

Figure 10: Results for A1, A2, A3, O1, O2 and O3: (a) overpressure with depth, (b) porosity reduction after tectonic compaction for cases A1, A2 and A3 relative to their respective parent cases O1, O2 and O3, (c) porosity with depth of cases A1, A2 and A3 compared to the NCT and the corrected NCT accounting for porosity loss due to tectonic compaction and (d) error resulting from the EDM predictions for A1, A2 and A3.

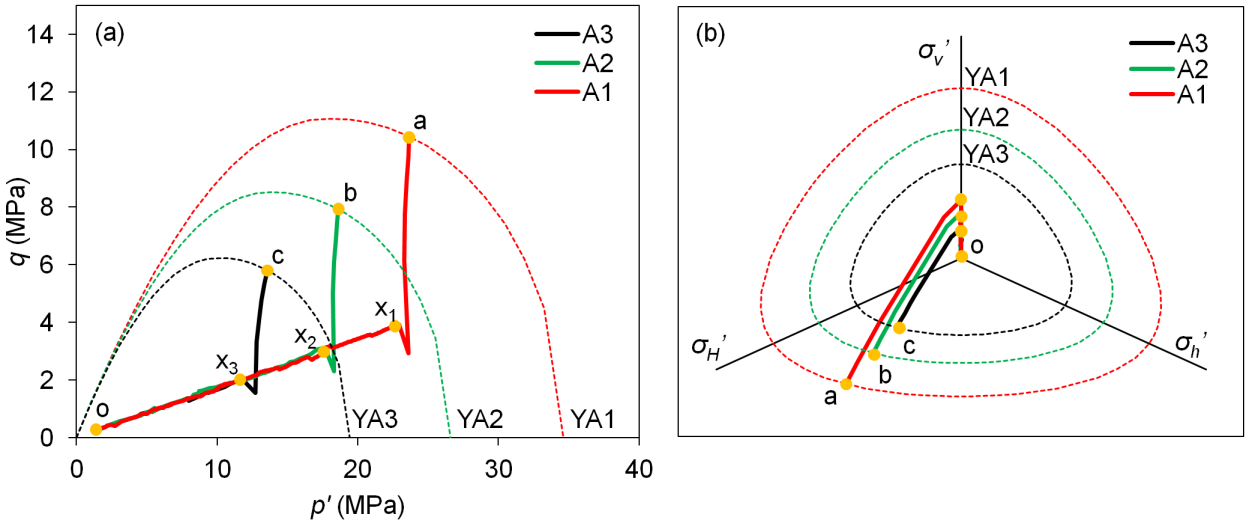

Figure 11: Results of cases A1, A2 and A3: (a) stress paths in the $p' - q$ plane and (b) stress paths in the deviatoric plane. The plots correspond to an element of rock situated at c.a. 2.8 km depth after sedimentation in each model. Point o is the initial stress state and x_1, x_2 and x_3 represent the stress states after the sedimentation stage of A1, A2 and A3, respectively (for the sake of clarity the labels are not displayed in (b)). Points a, b and c are the final stress states of cases A1, A2 and A3 respectively and YA1, YA2 and YA3 are their corresponding final yield surfaces. The stress paths are described as follows: [o-x_1/x_2/x_3] burial trend at K_0 conditions (different stress states are reached at the end of this stage and therefore different consolidation states), [x_1/x_2/x_3 - a/b/c] tectonic stress paths. Note that the large deviation from the K_0 in the final stress state of the case A1 compared with the final stress states of cases A2 and A3.

4.6. Effect of post tectonic burial

For the following results, a second period of sedimentation and burial subsequent to the tectonic event was considered. For cases D1, D2 and D3, a 500 m thick layer of sediment is deposited after the tectonic event at sedimentation rates of 100 m/Ma, 500m/Ma and 2000 m/Ma respectively. In all the cases, overpressures with depth are lower than the overpressures after the tectonic event (Fig. 12a). For cases D1 and D2 overpressures in depth are even lower than the case O2 (case with overpressure generated only by disequilibrium compaction). The predicted overpressures depend on the competing roles of overpressure dissipation due to the high overpressure magnitude after the tectonic event and overpressure generation due to disequilibrium compaction. As the last deposited layer is not affected by tectonics, the shallow porosities follow the original NCT and therefore no calibration is required for the application of the EDM (Fig. 12b). For all the cases the EDM error decreased relative to the parent case A2 (Fig. 12c). In fact for cases D1 and D2 the error is practically negligible and therefore the EDM give accurate predictions in these scenarios. This is because if post-tectonic burial is slow enough, the tectonic effect is overwhelmed and the VES-porosity relationships return to the 1D compaction trend (Fig. 12d). These results are in good agreement with the observations reported by Couzens-Schultz and Azbel (2014) in buried anticlines from the NW Borneo thrust belt. An analysis of the stress path for a point of rock located at 3.2 km depth reveals that cases D1 and D2 at present day are close to K_0 burial conditions (burial

conditions in absence of tectonic deformation) whereas the stress state for D3 at present day is still in the tectonic domain (Fig. 13).

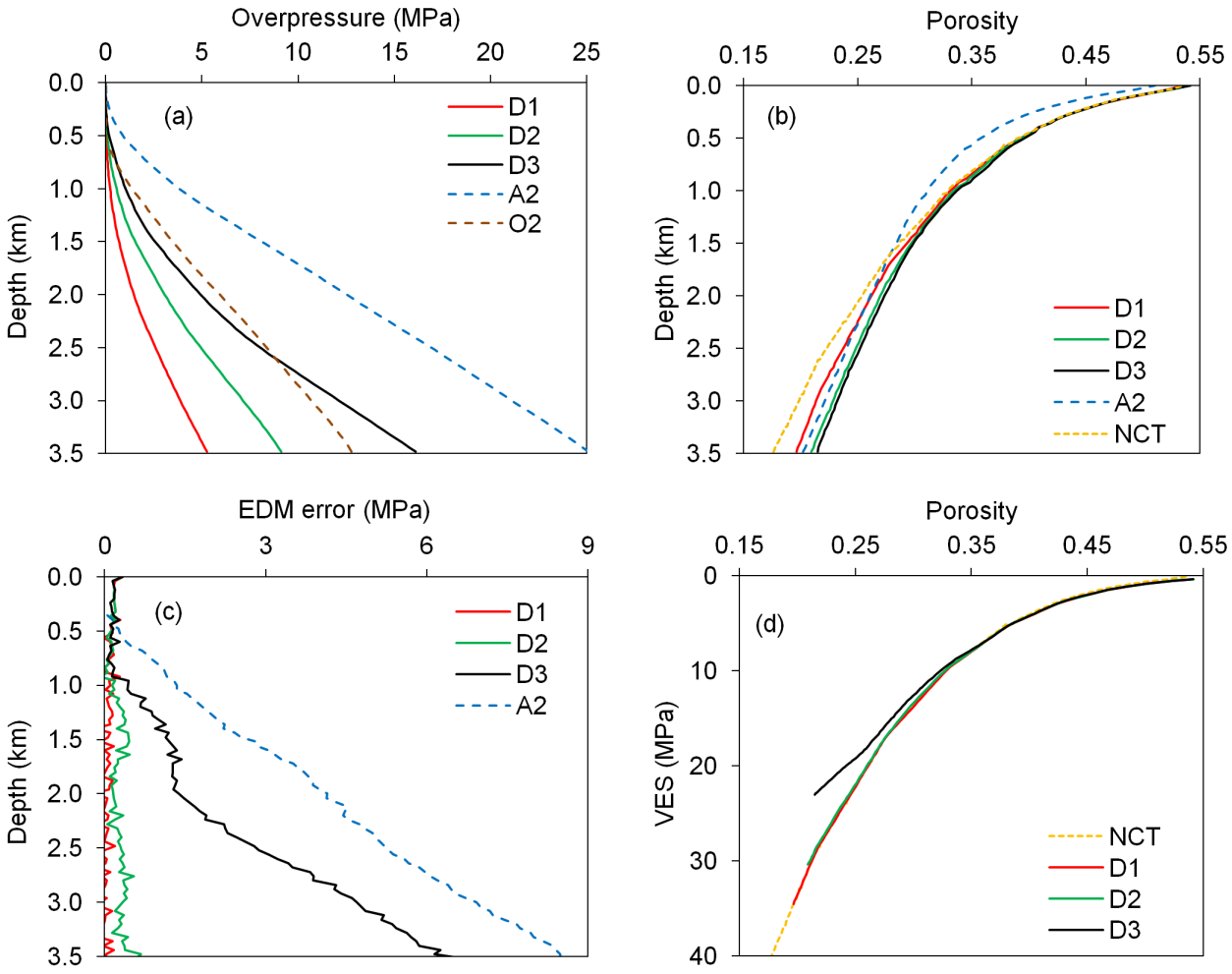

Figure 12: Results for cases D1, D2 and D3: (a) overpressure (cases O2 and A2 are plotted for reference), (b) porosity trends (NCT and A2 are plotted for reference). Note that the NCT does not require shifting to account for porosity loss due to tectonic compaction as the shallowest sediments are deposited after the tectonic event. (c) error resulting from EDM predictions and (d) VES - porosity relationships at depths of up 3.5 km compared to the NCT.

5. Discussion

This paper presents fully coupled geomechanical simulations with detailed analyses on the effect of tectonic compaction on stresses, porosity and overpressure. The adopted simple column geometry enabled us to eliminate the effects of complex basin architectures, geologic structures and stratigraphy contrasts on the solution, thus facilitating the understanding and interpretation of the results. Different basin histories have been investigated in order to assess their impact on the solution. Similar studies that used column geometries to investigate tectonic compaction have been performed by previous researchers. For example Luo (2004) used a one-dimensional finite

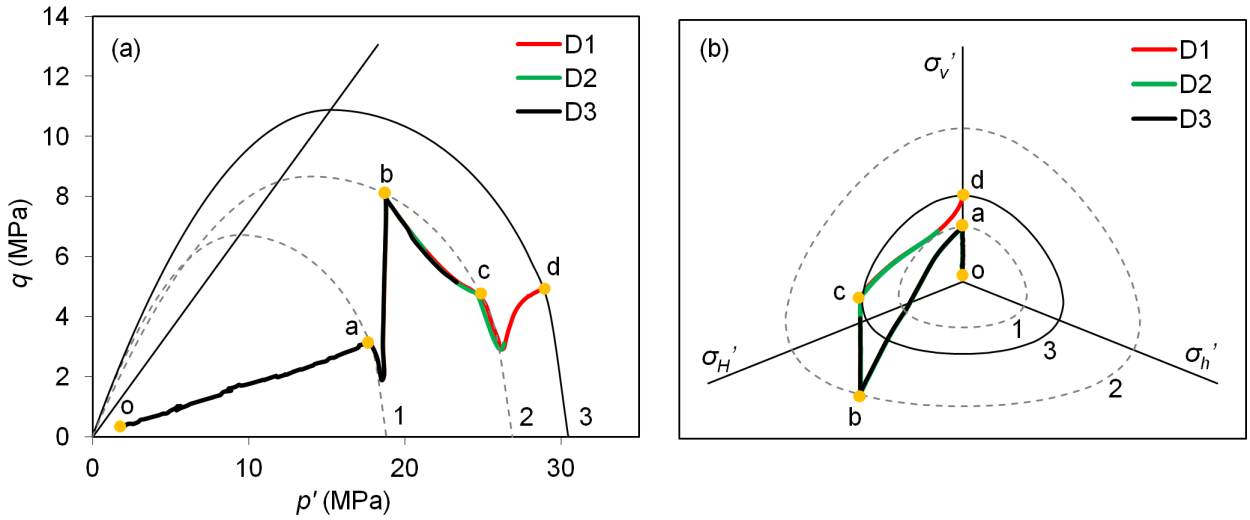

Figure 13: Results for cases D1, D2 and D3: (a) stress paths in $p' - q$ plane and (b) stress paths in the deviatoric plane. The numbers 1, 2 and 3 indicate the position of yield surface in the $p' - q$ plane and in the deviatoric plane for p' at the end of the sedimentation stage, the end of the tectonic event and the end of the post-tectonic sedimentation, respectively. The plots correspond to a point which is located at 3.2 km depth at the end of the post-tectonic sedimentation stage. The stress paths are described as follows: [o - a] burial trend at K_0 conditions, [a - b] tectonic stress paths, [b - c] elastic path of the post-tectonic sedimentation characterised by overpressure dissipation (the present day stress state of the case D3 does not reach the yield surface at point c), [c - d] plastic path of the post-tectonic sedimentation (the overpressure dissipation and the increase in effective stresses result in further plasticity. The path reaches the K_0 stress conditions at point d. Note that stress state of case D2 at the present day does not reach the K_0 condition).

element formulation to analyze the effect of the tectonic stress magnitude and the duration of the tectonic periods on the final overpressures and porosities. Maghous et al. (2014) presented 2D plane strain simulations comparing the effect of compressional and extensional tectonic events on columns under different states of consolidation. However, this paper presents a more extended study highlighting the coupled nature of stresses, compaction and overpressure in basins under different burial and tectonic histories that might be analogs of the bulk shortening occurring in field scenarios. The performed parametric study shows the influence of the amount of shortening, the shortening rate, the compaction and pressure state prior to the shortening and the rate of post tectonic burial on the sediment stresses, porosity and overpressure. Furthermore, the comparison of the overpressure predictions obtained from our models with predictions made by the EDM adds a valuable insight on the suitability of the traditional pore pressure prediction methods in tectonic environments.

Our models have predicted an overpressure increase of up to 16 MPa at 3.5 km depth and a loss of up to 6 porosity units due to the tectonic events. These results are within the bounds of field observations from shortening environments. For example, Couzens-Schultz and Azbel (2014) discussed the implications of tectonic compaction in the NW Borneo toe thrust. They stated that up to 10 porosity units might be lost by tectonic compaction in thrust environments. Their density data shows that the pre-kinematic sediments in the NW Borneo thrust belt systematically have a

greater density compared to the post-kinematic sediments for the same depth, thus evidencing the role of tectonic stress in compaction. In addition, they suggest that the compressive stresses in the NW Borneo thrust belt might have generated some overpressure in the low permeability strata, although no constraints on the magnitude are discussed. Furthermore, they presented conclusions which are in good agreement with the results of our models D1, D2 and D3: as sediments experience post-tectonic burial the compaction state returns to the 1D trend. Beaudoin et al. (2014) reaffirmed the significance of the tectonic deformation as an overpressure generation mechanism. They reconstructed the history of the paleo-fluid pressure in the Bighorn Basin and they pointed out that the overpressure gradually reached the lithostatic pressure during contraction and folding. In addition, they observed a coeval evolution between overpressure and differential stress indicating that both resulted from the compressional episode. This is also reflected in our models, which show a positive correlation of overpressure and deviatoric stress with the amount of shortening. More recently, Guo et al. (2016) postulated horizontal tectonic compression as the dominant overpressure generation mechanism in the Kela-2 anticlinal gas field located within the Tarim basin, NW China. They measured pore pressure in sandstones that are as high as 1.71 to 2.14 times the hydrostatic pressure.

The comparison of the overpressures predicted by our geomechanical models and those by the EDM clearly shows that the accuracy of the latter is significantly compromised in tectonic compressive scenarios. We have measured an EDM error magnitude of up to 11 MPa at a depth of 3.5 km. These results are not surprising as the EDM is based on a relationship between porosity and vertical effective stress, ignoring the contribution of lateral stresses on compaction and overpressure generation (Goulty, 2004; Hauser et al., 2014).

Despite the examples mentioned above, only a few publications highlight the contribution of tectonics on the overpressure observed in field scenarios. As noted by Yassir and Addis (2002), the recognition of tectonic compaction as an overpressure generation mechanism in the literature is well behind sedimentary loading, even in tectonically active regions. However, the results reported in this study clearly demonstrate that tectonic compaction deserves an important consideration in those basins in which it is identified as a potential overpressure generation mechanism and, consequently, pore pressure must be addressed carefully in those circumstances.

6. Conclusion

This study documents simulations of basins under different depositional and tectonic histories. The models consider up to three consecutive stages consisting of deposition, tectonic deformation and post tectonic burial. Sedimentation rates from 100 m/Ma to 2000 m/Ma and shortenings from

5% to 20% with displacement rates from 100 m/Ma to 400 m/Ma have been considered. From the numerical results it is concluded:

- Tectonic deformation leads to an overpressure increase and porosity decrease, which is contrary to the 1D compaction assumptions adopted by pore pressure prediction methods.
- In our simulations, the overpressure has increased up to 16 MPa at 3.5 km depth due to the tectonic deformation.
- A maximum porosity loss of 6 porosity units after tectonic compaction has been observed. However this amount is dependent on the tectonically induced overpressure and might increase if overpressure dissipation occurs.
- The tectonic deformation increases the horizontal effective stress and decreases the vertical effective stress due to an almost constant total vertical stress and an increase in the overpressure. This leads to a substantial increase in the deviatoric (differential) stress.
- After overburden correction to the tectonic effect in shallow sediment porosities the EDM has under predicted overpressure by up to 11 MPa
- The error obtained from the EDM prediction has shown to be dependent on the amount of shortening, the compaction and pressure state prior to the shortening and the rate of post tectonic burial whereas the deformation rate has shown no effect on it. The stress paths have revealed that the greater the deviation from the uniaxial burial trend, the less accurate is the EDM overpressure prediction.
- The tectonically induced overpressure is higher in basins with low porosities and low permeabilities.
- If enough post tectonic burial is present in the basin and the deposition rates are slow enough the tectonic effect might be overwhelmed and the conditions might return to the 1D compaction trend.

Acknowledgements These investigations were carried out as part of the GeoPOP3 project funded by BG, BP, Chevron, ConocoPhillips, DONG Energy, E.ON, ENI, Petrobras, Petronas, Statoil, Total and Tullow. We thank Brent Couzens-Schultz and an anonymous reviewer for constructive comments.

References

Albertz, M., Lingrey, S., 2012. Critical state finite element models of contractional fault-related folding: Part 1. Structural analysis. Tectonophysics 576-577, 133–149.

Albertz, M., Sanz, P. F., 2012. Critical state finite element models of contractional fault-related folding: Part 2. Mechanical analysis. Tectonophysics 576-577, 150–170.

Allwardt, J. R., Michael, G. E., Shearer, C. R., Heppard, P. D., Ge, H., 2009. 2D modeling of overpressure in a salt withdrawal basin, Gulf of Mexico, USA. Marine and Petroleum Geology 26 (4), 464–473.

Beaudoin, N., Lacombe, O., Bellahsen, N., Amrouch, K., Daniel, J. M., 2014. Evolution of pore-fluid pressure during folding and basin contraction in overpressured reservoirs: Insights from the MadisonePhosphoria carbonate formations in the Bighorn Basin (Wyoming, USA). Marine and Petroleum Geology 55 (8), 214–229.

Bekele, E. B., Johnson, M., Higgs, W., 2001. Numerical modelling of overpressure generation in the Barrow Sub-Basin, Northwest Australia. APPEA, 595–608.

Bera, P., 2010. Estimation of pore pressure from well logs: A theoretical analysis and case study from an offshore basin, North Sea. In: 8th Biennial International Conference and Exposition on Petroleum Geophysics. Vol. 76 of AAPG Memoir. Hyderabad, pp. 1–6.

Bolås, H. M. N., Hermanrud, C., Teige, G. M. G., 2004. Origin of overpressures in shales: Constraints from basin modeling. AAPG Bulletin 88, 193–211.

Brown, J. P., P., K., 2008. Pore pressure prediction as a prospecting tool, input to risk, volumes and field development. In: AAPG Annual Convention. Vol. 76 of AAPG Memoir. April 20-23, San Antonio, Texas, pp. 1–6.

Corredor, F., Shaw, J. H., F., B., 2005. Structural styles in the deep-water fold and thrust belts of the Niger Delta. AAPG Bulletin 89 (6), 753–780.

Cotecchia, F., Chandler, R. J., 1997. The influence of structure on the pre-failure behaviour of a natural clay. Géotechnique 47 (3), 523–544.

Couzens-Schultz, B. A., Azbel, K., 2014. Predicting pore pressure in active fold-thrust systems: An empirical model for the deepwater Sabah foldbelt. Journal of Structural Geology 69, 465–480.

Crook, A., Willson, S., Yu, J., Owen, D., 2006. Predictive modelling of structure evolution in sandbox experiments. Journal of Structural Geology 28 (5), 729–744.

Crook, A. J. L., 2013. ParaGeo: A Finite element model for coupled simulation of the evolution of geological structures. Three Cliffs Geomechanical Analysis, Swansea, UK.

Desai, C., Salami, M., 1987. A constitutive model and associated testing for soft rock. Int. J. Rock Mech. Min. Sci. 24, 299–307.

Goulty, N. R., 2004. Mechanical compaction behaviour of natural clays and implications for pore pressure estimation. Petroleum Geoscience 10 (1), 73–79–317.

Guo, X., Liu, K., Jia, C., Song, Y., Zhao, M., Lu, X., 2016. Effects of early petroleum charge and overpressure on reservoir porosity preservation in the giant Kela-2 gas field, Kuqa depression, Tarim Basin, northwest China. AAPG Bulletin 100 (2), 191–212.

Gutierrez, M., Wangen, M., 2005. Modeling of compaction and overpressuring in sedimentary basins. Marine and Petroleum Geology 22, 351–363.

Hantschel, T., Kauerauf, A., 2009. Fundamentals of basin and petroleum Systems Modeling, Berlin Edition. Vol. 11. Springer-Verlag.

Hashiguchi, K., 1995. Short communication on the linear relations of V-lnp' and lnv-*ln*p' for isotropic consolidation of soils. International Journal for Numerical and Analytical Methods in Geomechanics 19, 367–376.

Hauser, M. R., Couzens-Schultz, B. A., Chan, A. W., 2014. Estimating the influence of stress state on compaction behavior. Geophysics 79 (6), 389–398.

Hennig, A., Yassir, N., Addis, A., Warrington, A., 2002. Pore-pressure estimation in an active thrust region and its impact on exploration and drilling. In: A. R. Huffman and G. L. Bowers, eds. Pressure regimes in sedimentary basins and their prediction. Vol. 76 of AAPG Memoir. pp. 89–105.

Hubbert, M. K., Rubey, W. W., 1959. Role of fluid pressure in mechanics of overthrust faulting i. mechanics of fluid-filled porous solids and its application to overthrust faulting. Geological Society of America Bulletin 70 (2), 115–166.

Krueger, S. W., Grant, N. T., 2011. The growth history of toe thrusts of the niger delta and the role of pore pressure. In: Thrust Fault-Related Folding. Vol. 94 of AAPG Memoir. McClay, K., Shaw, J. & Suppe, J., pp. 357–390.

Lewis, R. W., Schreffler, B. A., 1998. The finite element method in the static and dynamic deformation and consolidation of porous media. Wiley.

Luo, G., Nikolinakou, M., Flemings, P., Hudec, M., 2012. Geomechanical modeling of stresses adjacent to salt bodies: Part - Uncoupled models. AAPG Bulletin 96 (1), 43–64.

Luo, X., 2004. Quantitative analysis on overpressuring mechanism resulted from tectonic stress. Chinese Journal of Geophysics 47 (6), 1223–1224.

Maghous, S., Bruch, A., Bernaud, D., Dormieux, L., Braun, A. L., 2014. Two-dimensional finite element analysis of gravitational and lateral driven deformation in sedimentary basins. Int. J. for Num. and Anal. Meth. Geomech. 38, 725–746.

Neumaier, M., Littke, R., Hantschel, T., Maerten, L., Joonnekindt, J. P., Kukla, P., 2014. Integrated charge and seal assesment in the Monagas fold and thrust belt of Venezuela. AAPG Bulletin 98 (7), 1325–1350.

Nikolinakou, M. A., Luo, G., Hudec, R., M., Flemings, P. B., 2012. Geomechanical modeling of stresses adjacent to salt bodies: Part 2 - Poroelastoplasticity and coupled overpressures. AAPG Bulletin 96 (1), 65–85.

Obradors-Prats, J., Rouainia, M., Aplin, A. C., Crook, A. J. L., 2016. Stress and pore pressure histories in complex tectonic settings predicted with coupled geomechanical-fluid flow models. Marine and Petroleum Geology 76, 464–477.

Osborne, M. J., Swarbrick, R. E., 1997. Mechanisms for generating overpressure in sedimentary basins: A re-evaluation. AAPG Bulletin 81, 1023–1041.

Peric, D., Crook, A., 2004. Computational strategies for predictive geology with reference to salt tectonics. Computer Methods in Applied Mechanics and Engineering 193 (48-51), 5195–5222.

Rouainia, M., Muir Wood, D., 2000. An implicit constitutive algorithm for finite strain Cam clay elasto-plastic model. Mechanics of Cohesive-Frictional Materials 5 (6), 469–489.

Schneider, F., Hay, S., 2001. Compaction model for quartoze sandstones applicattion to the Gran ormation, Haltenbanken, Mid-Norwegian Continental Shelf. Tectonophysics 18 (7), 3833–848.

Schneider, F., Potdevin, J. L., Wolf, S., Faille, I., 1996. Mechanical and chemical compaction model for sedimentary basin simulators. Tectonophysics 263 (1-4), 307–317.

Smart, K. J., Ferrill, A., D., Morris, A. P., N., M. R., 2012. Geomechanical modeling of stress and strain evolution during contractional fault-related folding. Tectonophysics 576-577, 171–196.

Swarbrick, R. E., 2002. Challenges of porosity-based pore pressure prediction. CSEG Recorder, 75–78.

Swarbrick, R. E., Osborne, M. J., Yardley, G. S., 2002. Modeling of compaction and overpressuring in sedimentary basins. Marine and Petroleum Geology 22, 351–363.

Terzaghi, K., 1967. Soil Mechanics in Engineering Practice. John Wiley & Sons.

Thornton, D. A., Crook, A. J. L., 2014. Predictive modelling of the evolution of fault structure: 3D modelling and coupled geomechanical/flow simulation. Rock Mechanics and Rock Engineering 47 (5), 1533–1549.

Van Ruth, P., Hillis, R., Swarbrick, R., 2002. Detecting overpressure using porosity-based techniques in the Carnarvon Basin, Australia. APPEA Journal, 559–569.

Ventouras, K., Coop, M. R., 2009. On the behaviour of thanet sand: An example of an uncemented natural sand. Géotechnique 59, 727–738.

Wangen, M., 2001. A quantitative comparison of some mechanisms generating overpressure in sedimentary basins. Tectonophysics 334, 211–234.

Wood, D. M., 1990. Soil Behaviour and Critical State Soil Mechanics. Cambridge University Press.

Yang, Y., Aplin, A. C., 2004. Definition and practical application of mudstone porosity-effective stress relationships. Petroleum Geoscience 10, 153–162.

Yang, Y., Aplin, A. C., 2010. A permeability-porosity relationship for mudstones. Marine and Petroleum Geology 27 (8), 1692–1697.

Yassir, N., Addis, M. A., 2002. Relationships between pore pressure and stress in different tectonic settings. Pressure regimes in sedimentary basins and their prediction. In: A. R. Huffman and G. L. Bowers, eds. Pressure regimes in sedimentary basins and their prediction. Vol. 76 of AAPG Memoir. pp. 79–88.

Zhang, J., 2011. Pore pressure prediction from well logs: Methods, modifications, and new approaches. Earth-Science Reviews 108 (1-2), 50–63.

List of Figures